

Photonic force microscopy of surface electromagnetic waves in a one-dimensional photonic crystal

Daniil A. Shilkin^a, Evgeny V. Lyubin^a, Irina V. Soboleva^{a,b}, and Andrey A. Fedyanin^a

^aFaculty of Physics, Lomonosov Moscow State University, 119991 Moscow, Russia

^bA. N. Frumkin Institute of Physical Chemistry and Electrochemistry,
Russian Academy of Science, Moscow 119071, Russia

ABSTRACT

The potential of photonic force microscopy (PFM) to directly probe the field of the Bloch surface wave (BSW) in a one-dimensional photonic crystal is considered. Optical forces acting on a dielectric microparticle in the evanescent field of the BSW are estimated in the dipole approximation and calculated by finite-difference time-domain (FDTD) analysis. Technical details of the PFM measurements are described.

Keywords: photonic crystals, surface electromagnetic waves, photonic force microscopy

1. INTRODUCTION

Optical manipulation has been commonly used in nano- and microscience since the optical tweezers technique was firstly demonstrated by Ashkin in 1986.¹ Properties of single biological cells^{2–4} and macromolecules,^{5–7} electric^{8,9} and magnetic^{10,11} interactions of colloidal particles are just a few of the subjects studied with the use of optical tweezers. By means of diffractive optical elements, rapid-scanning mirrors or spatial light modulators one can create an array of optical traps and manipulate a large number of particles simultaneously.^{12–14} However, being a powerful method for single particle investigation, the optical tweezers manipulation technique is not optimal for integration on microfluidic devices. As an alternative to optical tweezers, manipulation by evanescent fields allows sorting, trapping and transfer of a large number of particles at fine linear or planar field confinement.¹⁵ To date, manipulation in such a way has been realized using total internal reflection (TIR)^{16–18} and surface plasmon polariton (SPP)^{19–21} evanescent fields, photonic crystal cavities^{22,23} and plasmonic nanostructures.²⁴ To the best of our knowledge, multilayer photonic crystals have not been used for optical manipulation so far, in spite of its fabrication simplicity and low energy loss.

Surface electromagnetic waves in photonic crystals, also known as Bloch surface waves (BSWs), are surface electromagnetic modes that propagate in all-dielectric structures and provide large local field enhancement.^{25,26} Due to its high quality factor, BSWs are widely used for sensing applications.^{27–29} Similar to plasmonic waveguides, multilayer photonic crystals are also considered as a possible platform for two-dimensional integrated optics. BSW refraction, reflection and focusing schemes have been realized by depositing of flat polymer structures on a one-dimensional photonic crystal surface.^{30,31}

To study force interactions acting at the microscale, photonic force microscopy (PFM)^{32,33} is broadly used. This technique uses analysis of particle displacements in an optical tweezers trap to determine external forces acting on the particle. Forces acting on polystyrene microbeads in the TIR³⁴ and SPP³⁵ evanescent fields have been measured by means of PFM.

In this work, the potential of PFM to directly probe the field of the BSW in a dielectric multilayer is considered. Numerical calculations of the force induced by the BSW are carried out in the dipole approximation and by finite-difference time-domain (FDTD) simulation. Measurements of forces acting on a 1- μm polystyrene bead in the evanescent field of the BSW are performed. Technical details of the PFM measurements are described. Special attention is given to the calibration process.

Further author information: (Send correspondence to Daniil Shilkin) E-mail: shilkin@nanolab.phys.msu.ru

2. THEORETICAL CONSIDERATIONS

To obtain a large value of the optical force, one has to provide a large electromagnetic field gradient that can be done either by increase of the laser power or the field localization degree. The penetration depth of all of the in-plane evanescent waves (TIR, SPP and BSW) depends on the excitation scheme parameters, but is always about several hundred nanometers, whereas the field enhancement differs a lot between them. The typical values of the ratio of the field strength in the evanescent wave to that one in the excitation radiation are: 1 for the TIR wave, about 6 for the SPP one, and as large as 20 in case of the BSWs. The SPP-induced optical forces exceed the TIR-induced ones by more than an order of magnitude.³⁶ So one can expect the BSW-induced forces to exceed the SPP-induced ones significantly too.

In this section, the BSW excitation conditions and field enhancement are discussed, the gradient component of the BSW-induced optical force is calculated in the dipole approximation, and the results are compared with the ones of numerical simulation.

2.1 Surface Wave Excitation and Field Enhancement

To calculate electromagnetic field propagating in the photonic crystals, the transfer matrix technique was used. The optimal thickness and number of layers were firstly determined by comparison of the field enhancement calculated for different parameters and then used for the photonic crystals fabrication. The actual refractive indices of the component materials and the layer thicknesses of the fabricated samples were determined by the ellipsometry technique. All of the presented calculation results have been obtained using these data.

As the component materials of the photonic crystals, zirconium and silicon oxides were used. These materials are quite suitable because of the large difference in refractive index and acceptable expansion factors. For the BSW excitation, radiation with wavelength of 532 nm was used in the experiments. At this wavelength, the refractive indices of zirconium and silicon oxides are 1.91 and 1.46, respectively. Fabricated photonic crystals consist of 5 pairs of layers with thicknesses about $\lambda/4n$, where n is the refractive index of the layer material and $\lambda = 1200$ nm is the central wavelength of the photonic crystal band gap. The multilayer is deposited on a glass substrate with refractive index of 1.52. The BSW is excited in the Kretschmann configuration at the interface between the photonic crystal and water.

Fig. 1a shows calculated reflectance for the photonic crystal illuminated with *s*-polarized radiation in the Kretschmann geometry as a function of wavelength and angle of incidence in the glass substrate. As the angle of incidence increases, the band gap shifts to the blue. When total internal reflection is achieved at the angle of about 61° , a narrow dip appears in the band gap region corresponding to the BSW excitation.

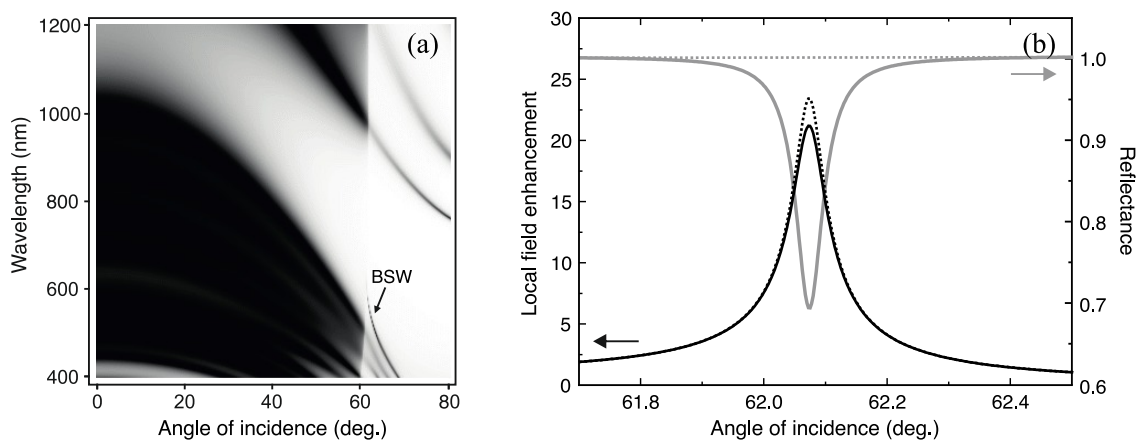


Figure 1. (a) Calculated reflectance of the photonic crystal as a function of wavelength and angle of incidence of *s*-polarized light in the Kretschmann configuration. Bright regions correspond to high reflectance. (b) Angular dependences of local field enhancement (black) and reflectance (grey) at 532 nm calculated for non-absorptive materials (dotted) and for materials with absorption coefficients of $3 \cdot 10^{-5}$ (solid). Angle of incidence is defined in the glass substrate.

When calculating reflectance spectra for BSW excitation by the transfer matrix technique, one need to introduce a non-zero absorption, otherwise total reflectance is obtained even at the BSW resonance conditions. In fact, the BSW excitation leads to a decrease of the reflectance at least partly because of the BSW scattering at surface roughness. To take this into account we introduce an effective absorption coefficients and choose them to be $3 \cdot 10^{-5}$ for all of the materials. The results obtained with and without absorption are compared in Fig. 1b.

When the BSW is excited in a photonic crystal, electromagnetic field is localized close to its surface and decays exponentially behind the photonic crystal: $E \propto e^{-|z|/d_p}$. The magnitude of electric field at the surface is shown in Fig. 1b by black line as a function of angle of incidence of the excitation radiation. The values are in units of electric field magnitude in the incident light. As one can see the field enhancement L at the BSW resonance is about 20. The penetration depth d_p into water does not depend on the BSW excitation and is calculated as the inverse of the imaginary part of the normal wave vector component:

$$d_p = \frac{1}{\sqrt{(2\pi n_g/\lambda)^2 \sin^2 \theta - (2\pi n/\lambda)^2}}, \quad (1)$$

where λ is the wavelength in vacuum, $n = 1.33$ is the refractive index of water, $n_g = 1.52$ is the refractive index of glass and $\theta \sim 62^\circ$ is the angle of incidence of the excitation radiation in glass. At our experimental conditions, the penetration depth $d_p \sim 450$ nm.

2.2 Gradient Force in the Dipole Approximation

Optical radiation forces exerted on transparent particles are commonly divided into the scattering and the gradient components. The first one is directed along the wave vector of light and causes particle propulsion. The second one is directed along the intensity gradient and is used for optical trapping. In case of BSW-induced force, the scattering component is directed in the BSW propagation direction and the gradient one is perpendicular to the photonic crystal surface as it is shown in Fig. 2.

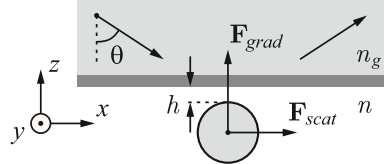


Figure 2. Schematic of the problem. A dielectric particle is located in water (refractive index n) close to the photonic crystal surface. Light is incident from glass (refractive index n_g) exciting BSWs at the photonic crystal surface. The BSW-induced optical forces pull the particle to the surface and push it in the BSW propagation direction.

To estimate the optical gradient force acting on a dielectric microparticle in a highly localized electromagnetic field, the dipole approximation can be used for any particle size.³⁷ In this approach the energy of interaction between a particle and an electromagnetic field is calculated by integrating the unperturbed field intensity over the particle volume:

$$W = -\frac{1}{4} \int \alpha E^2 d\mathbf{r}, \quad (2)$$

where $E = E(\mathbf{r})$ is the electric field amplitude and α is the specific polarizability. In case of a spherical particle it is calculated as follows:

$$\alpha = \frac{3}{4\pi} \frac{m^2 - 1}{m^2 + 2}, \quad (3)$$

where m is the ratio of the refractive index of the particle to that of the surrounding medium.

The optical gradient force is then calculated as the gradient of W :

$$\mathbf{F}_{grad} = -\nabla W. \quad (4)$$

In the evanescent field of BSW $E(z) = L(8\pi I/n_g c)^{1/2} e^{-|z|/d_p}$ where I is the intensity of the excitation light, one can obtain an exact solution of the problem in the dipole approximation:

$$F_{grad} = \frac{dW}{dh} = \frac{3\pi}{4} \frac{(m^2 - 1)}{(m^2 + 2)} \frac{L^2 I}{n_g c} K(\kappa, a) e^{-2\kappa h}, \quad (5)$$

where

$$K(\kappa, a) = \frac{(\kappa a + 1)e^{-2\kappa a} + (\kappa a - 1)}{\kappa^2}, \quad \kappa = 1/d_p = \frac{2\pi}{\lambda} \sqrt{n_g^2 \sin^2 \theta - n^2}, \quad (6)$$

and a is the bead diameter.

In our experiments, an excitation beam is used with the angular divergence of much higher value than the width of the BSW resonance. For this reason one needs to expand the excitation radiation into plane waves when calculating the BSW-induced optical force. In case of a Gaussian beam with radius of w_0 , the intensity of the mode i is calculated as follows:

$$I_i \propto \exp\left(-2(\theta_i - \theta_0)^2 / \Theta^2\right), \quad (7)$$

where $\Theta = 2\lambda/\pi n_g w_0$ is the angular divergence of the beam. The expression (5) is then transformed to

$$F_{grad} = \frac{3\pi}{4} \frac{(m^2 - 1)}{(m^2 + 2)} \sum_i \frac{L^2(\theta_i) I_i}{n_g c} K(\kappa(\theta_i), a) e^{-2\kappa(\theta_i) h}. \quad (8)$$

Fig. 3 presents the results of calculations in the dipole approximation. In the calculations, the particle diameter was set to be $1\mu\text{m}$, its effective refractive index was the ratio of the ones of polystyrene and water $m = 1.59/1.33$, and the gap between the bead and the surface $h = 100\text{ nm}$.

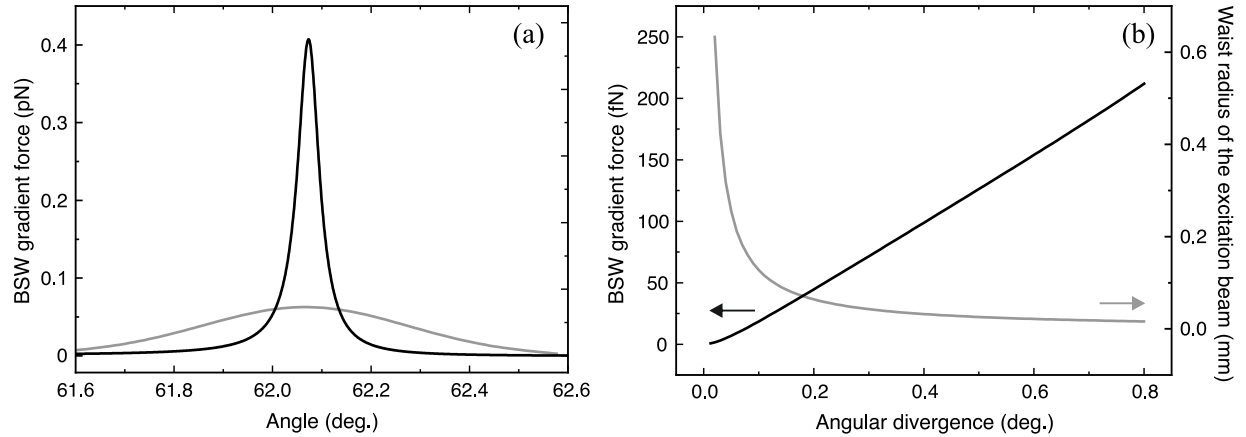


Figure 3. (a) BSW gradient force calculated in the dipole approximation as a function of angle of incidence of the excitation radiation for plane wave excitation (black) and for angular divergence of $\Theta = 0.4^\circ$ (grey). In both cases, the intensity of the excitation beam is 1 kW/cm^2 . (b) Dependences of the BSW gradient force (black) at fixed excitation power of 50 mW and the waist radius of the excitation light beam (grey) on its angular divergence. The particle diameter $a = 1\mu\text{m}$, its effective refractive index $m = 1.59/1.33$, the gap between the surface and the particle $h = 100\text{ nm}$.

In Fig. 3a the angular dependences of the BSW gradient force are shown obtained by (5) for plane wave excitation and by (8) for angular divergence of $\Theta = 0.4^\circ$ which is close to that in our experiments. In both cases, the intensity of the excitation beam is 1 kW/cm^2 . Being much smaller than for plane-wave excitation of the same intensity, the BSW-induced gradient forces are still large enough to be measured by PFM.

One can achieve a smaller divergence angle by increasing the beam diameter. However, the intensity of the radiation decreases and the force is not enhanced at that as it is evident from Fig. 3b.

2.3 FDTD Simulation

To obtain the exact values of the BSW-induced optical forces acting on a dielectric particle, one need to find out how the particle perturbs the BSW electromagnetic field. For that, finite-difference time-domain (FDTD) analysis can be used. The optically induced forces can be then calculated by integrating the Maxwell stress tensor (MST) over a closed surface enclosing the particle.

For FDTD analysis we used Lumerical FDTD Solutions 8.9.231. The propagation of a broad-spectrum pulse in the BSW mode in the presence of a $1\text{-}\mu\text{m}$ polystyrene bead was simulated and the Fourier component was found corresponding to the wavelength of 532 nm . Fig. 4a presents the results of the simulation at the surface/particle gap of 100 nm . The BSW propagates from the left to the right scattering at the particle and inducing the force.

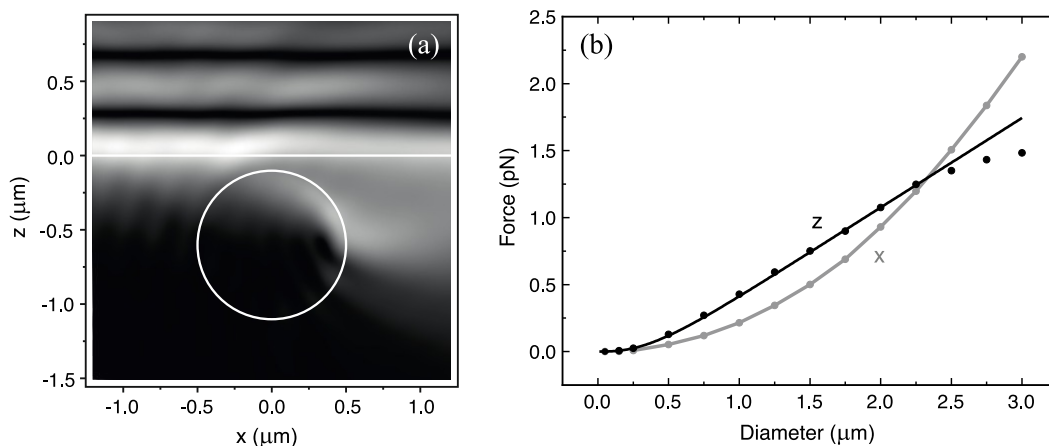


Figure 4. (a) Electric field distribution calculated by FDTD simulation. White line at $z = 0$ corresponds to the bottom side of the photonic crystal, white circle shows the particle contour. Bright regions correspond to high electric field magnitude. (b) Dependences of the BSW-induced force on a polystyrene bead in x -direction calculated by FDTD (grey), and in z -direction calculated by FDTD (black dots) and in the dipole approximation (black line). The surface/particle gap $h = 100\text{ nm}$; the intensity of the plane wave excitation is 1 kW/cm^2 .

The BSW-induced force was calculated by MST analysis. The results obtained for different particle sizes are shown in Fig. 4b by dots. It is interesting to compare the results of the numerical analysis with the ones of the dipole approximation. The BSW-induced gradient force calculated in the dipole approximation is shown in Fig. 4b by black line. As one can see the results are in excellent agreement with the ones of the numerical simulation while the particle diameter is less than $2\text{ }\mu\text{m}$.

3. EXPERIMENTAL TECHNIQUE

In this section, our PFM technique is described. To perform precise measurements by PFM, one needs to calibrate optical tweezers taking into account the vicinity of the surface. The difficulties which arise in this case are discussed and the technique applied in our experiments is described in detail.

3.1 Photonic Force Microscopy Setup

The optical tweezers setup used in our PFM experiments is shown in Fig. 5. The optical trap is formed by the radiation of a fiber-pigtailed single-mode laser diode 1 emitting a wavelength of 975 nm . The power of the laser output is set to about 0.1 W . The output light is collimated by an aspheric lens 2 with focal length of 18.4 mm into a parallel beam of 3.8 mm diameter. The lens is covered with an infrared antireflection coating. A neutral optical filter 3 of 10% transmission is used to prevent the light reflected from the sample from entering the resonator and so to increase the power stability of the laser radiation.

The collimated beam is expanded with an aspheric lens 4 ($f=25\text{ mm}$) and a doublet of a positive meniscus lens 5 and a biconvex lens 6. The use of such a doublet allows us to reduce aberrations significantly. The focal

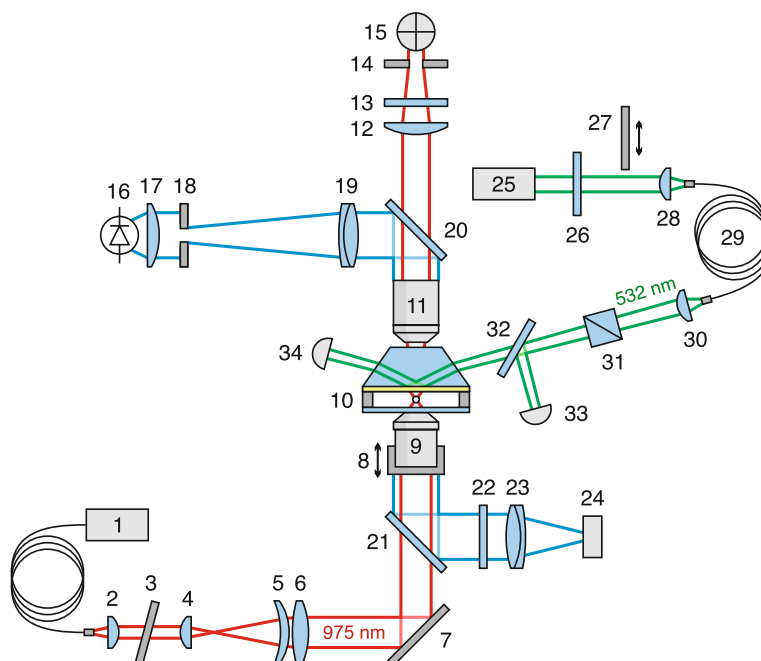


Figure 5. (color online) Experimental setup. 1 — fiber-pigtailed single-frequency laser diode (532 nm); 2,4-6,12,17,19,23,28,30 — lenses; 3 — neutral optical filter; 7 — mirror; 8 — mechanical and piezo translation stage; 9,11 — objective lenses; 10 — sample; 13,20,21 — dichroic optical filters; 14,18 — iris diaphragms; 15 — quadrant photodiode; 16 — LED; 22 — absorptive optical filters; 24 — CMOS imaging sensor; 25 — frequency-doubled Nd-YAG laser (532 nm); 26 — half wave plate; 27 — electromechanical shutter; 29 — single-mode polarization-preserving optical fiber; 31 — Glan prism; 32 — glass plate; 33,34 — photodiodes.

length of both lenses in the doublet is about 150 mm. Each of the beam expander lenses is covered with an antireflection coating.

After expansion and reflecting from a mirror 7, the beam is focused by a water-immersion objective lens 9 Olympus UPlanSApo 60XW with NA of 1.2 inside a cell 10 filled with water suspension of polystyrene microbeads of 1- μm diameter. The cell consists of two cover glasses with refractive index of 1.52 and thickness of about 0.15 mm separated by friction tape of 0.2 mm thickness. The bottom side of the upper glass is covered with a photonic crystal sample. To avoid adhesion between the microparticles and the photonic crystal surface, sodium dodecyl sulfate (SDS) is added that is a commonly used surfactant. The concentration of SDS in the suspension is 10 mM which is slightly more than the critical micelle concentration.

The cell is placed on a horizontal stage that allows one to manipulate the sample position relative to the beam axis. The vertical position of the waist is controlled by a mechanical and piezo translation stage 8 on which the objective lens is mounted. The trap position can also be manipulated in three dimensions by moving the lens 4.

The radiation scattered at a particle in the optical tweezers trap is condensed by an objective lens 11 with focal length of 16 mm and NA of 0.5. The position of the microparticle inside the trap is determined using a quadrant photodiode (QPD) 15 on which an image of the back focal plane of the objective 11 is formed by a 60-mm biconvex lens 12. The QPD signals are digitized with sampling rate of 50 kHz. Dichroic optical filters 13 are used to prevent visible radiation from reaching the QPD.

To visualize the particles, we use standard transmitted light optical microscopy technique. The radiation of an LED 16 used for illumination is collimated by an aspheric lens 17 ($f = 20$ mm) and passes through a field diaphragm 18 placed in the focal plane of an achromatic doublet 19 ($f = 200$ mm). An image of the field aperture

is formed in the cell by the objective 11 providing uniform illumination of the particles. The field of view of the immersion objective 9 is projected onto a CMOS imaging sensor 24 by an achromatic doublet 23 with focal length of 60 mm. To prevent laser radiation from reaching the camera, we use absorptive optical filters 22. In the setup, infrared and visible light are divided by dichroic mirrors 20 and 21.

The BSW excitation is realised in the Kretschmann attenuated-total-internal reflection configuration by using a prism of dense flint glass with angle of 54.6° and refractive index of 1.66. Optical contact between the prism and the photonic crystal sample is maintained by immersion oil. For the BSW excitation, the radiation of a frequency-doubled Nd-YAG laser 25 at 532 nm is used. The polarization is controlled by a half-wave plate 26. An electromechanical shutter 27 is used to turn the BSW excitation on and off. The Gaussian mode is selected by a single-mode polarization-preserving optical fiber 29 with NA of 0.12 and mode field diameter of $3.3\ \mu\text{m}$. To couple the laser beam into the fiber an aspheric lens 28 ($f = 11\ \text{mm}$) is used. At the fiber output, the laser radiation is focused on the photonic crystal sample by an aspheric lens 30 ($f = 4.5\ \text{mm}$) into a spot of about $70\text{-}\mu\text{m}$ diameter. The divergence angle in the glass substrate is 0.4° . The beam power at the fiber output is about 60 mW which corresponds to the intensity of $1.6\ \text{kW}/\text{cm}^2$ at the photonic crystal. A Glan prism 31 is used to additional polarization filtering. The intensity of the radiation beam is controlled by a photodiode 33 on which the beam is directed with a glass plate 32. To measure the reflectance of the photonic crystal, a photodiode 34 is used. Components 30–33 are mounted on a rotation stage to control the angle of incidence of the excitation radiation.

The photonic crystals used in this work have been made by thermal vacuum deposition. 5 pairs of layers of ZrO_2 and SiO_2 have been deposited on a glass substrate with refractive index of 1.52. The transmittance spectrum of a photonic crystal sample measured at normal incidence is given in Fig. 6 by dots, the calculated one is shown by line. The dip at 1200 nm corresponds to the first band gap, the dip near 400 nm corresponds to the second one.

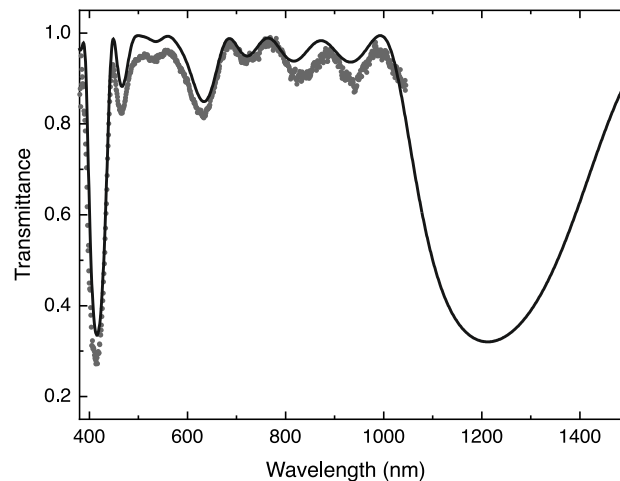


Figure 6. Experimental (dots) and calculated (line) transmittance spectra of the PC sample at normal incidence. The dip at 1200 nm corresponds to the first band gap, the dip near 400 nm corresponds to the second one.

3.2 Calibration and Data Analysis

The calibration process consists of a few steps. At the first step, the piezoelectric stage was calibrated by mechanical translation. By means of the piezoelectric stage the position of the trapping beam waist can be controlled with nanometer accuracy. However during long measurements, the photonic crystal surface can change its position causing significant uncontrollable changes of the distance between the particle and the surface.

To stabilize the particle position relative to the photonic crystal surface during the PFM measurements, the following technique is used. At first, the dependence of the average QPD sum signal on the position of the

trapping beam waist is measured. A typical example of that is shown in Fig. 7. Every point in the plot is obtained within 5 s which is much more than the characteristic time of thermal motion in our experiments 0.1 s. On the left side of the plot the waist of the trapping beam is located above the bottom side of the photonic crystal, the particle is pressed to the surface and displaced down from the trap. As the waist approaches the surface, its displacement decreases and the QPD signal rises. On the right of the plot the waist is located inside the cell and the particle is trapped close to the beam waist. In this case the equilibrium position relative to the waist center is not changed significantly with the waist displacement and the average QPD signal remains almost constant. Slight changes of the particle position inside the trap are caused by reflection of the trapping beam from the photonic crystal and the presence of SDS in the suspension.

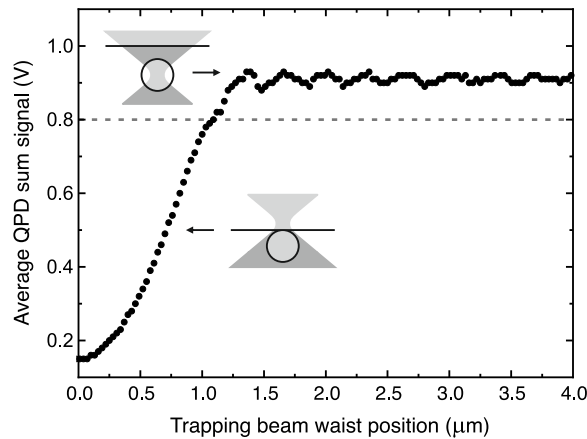


Figure 7. Average QPD sum signal as a function of the trapping beam waist position. On the left side of the plot, the waist of the trapping beam is located above the bottom side of the photonic crystal, the particle is pressed to the surface and displaced down from the trap. On the right, the waist is located inside the cell and the particle is trapped close to the beam waist.

After the dependence is obtained, the particle position relative to the photonic crystal surface can be stabilized as follows. The waist is initially located inside the cell and the particle is trapped close to the waist center. Then the waist approaches the surface until the average QPD sum signal becomes as small as a certain established value. In Fig. 7 a possible value for this parameter is shown by dashed line. After this value is exceeded, the waist is translated a desired distance inside the cell.

During the measurements, this procedure is repeated every minute providing a constant average value of the distance h between the surface and the equilibrium particle position. It is important to notice that one cannot determine just by the described procedure what the actual distance is between the particle and the surface. Moreover, changing the waist position by a certain value does not guarantee changing the particle equilibrium position by the same value at least partly because of reflection of the trapping beam from the photonic crystal disturbing the optical potential.^{38,39} For this reason the distance h between the particle and the surface should be determined independently for every waist position.

When measuring forces by optical tweezers, one usually need to know two parameters per axis. While the particle displacements are small, the trap potential is harmonic and the force acting on a trapped particle is proportional to displacement of the particle equilibrium position. The coefficient of proportionality k called the trap stiffness is the first parameter one needs to obtain by calibration. The second parameter is the coefficient S of proportionality between the particle displacement and the corresponding change of the QPD signal.

The standard optical tweezers calibration technique allows one to obtain the trap stiffness k and the coefficient S by measuring the power spectrum of the QPD signal.⁴⁰ In a harmonic potential, the two-sided power spectral density of the particle coordinate x is

$$G_x(f) = \frac{D/(2\pi^2)}{f_c^2 + f^2}, \quad (9)$$

where $D = k_B T / \gamma$ is the diffusion coefficient, $f_c = k / (2\pi\gamma)$ is the corner frequency, k_B is the Boltzmann constant, T is the temperature and γ is the hydrodynamic drag. If one supposes $x = S V$ where V is the QPD signal, the two-sided power spectral density of the QPD signal is calculated as follows:

$$G_V(f) = S^{-2} \frac{D/(2\pi^2)}{f_c^2 + f^2}. \quad (10)$$

Approximating experimental power spectra by (10) allows one to obtain S and k for each of the coordinate axes.

When the particle is trapped in the vicinity of a surface, the hydrodynamic friction depends on the distance between the surface and the particle and (10) should be transformed:

$$G_V(f) = S^{-2} \frac{D(h)/(2\pi^2)}{f_c^2(h) + f^2}, \quad (11)$$

where

$$D(h) = \frac{\xi(h)k_B T}{\gamma}, \quad f_c(h) = \frac{k(h)\xi(h)}{2\pi\gamma}. \quad (12)$$

The coefficient $\xi(h)$ in case of motion parallel to the surface is calculated as follows:⁴¹

$$\xi_{x,y}(h) = 1 - \frac{9}{16} \left(\frac{a}{a+2h} \right) + \frac{1}{8} \left(\frac{a}{a+2h} \right)^3 - \frac{45}{256} \left(\frac{a}{a+2h} \right)^4 - \frac{1}{16} \left(\frac{a}{a+2h} \right)^5. \quad (13)$$

The same coefficient in case of motion perpendicular to the surface is

$$\xi_z(h) = \frac{12h^2 + 2ah}{12h^2 + 9ah + a^2}. \quad (14)$$

In our measurements, the coefficient S is suggested to be independent of the waist position and its value can be determined either far away from the surface or by extrapolation of values obtained at different waist positions. The coefficients k and h can be then determined for every waist position by approximation of single power spectra by (11).

4. RESULTS AND DISCUSSION

The PFM measurements described below were partly automated by LabVIEW 2012. At the beginning, the waist position is manually set inside the cell at the distance of about $1 \mu\text{m}$ from the surface. Then the waist positioning relative to the surface is automatically performed as described above and the first measurement series begins.

Every measurement series consist of three steps. At the first one, data from the QPD are collected during 10 s at the closed position of the shutter 27 (see Fig. 5). Then the shutter is automatically opened and the data are collected during 20 s. At the last step, the shutter is closed again and the data are collected during 10 s. After the series is completed, the waist positioning procedure is performed and the next series begins.

The QPD sum signal measured at the BSW resonance conditions is demonstrated in Fig. 8a. The increase of the signal when the BSW is excited corresponds to the particle displacement towards the surface. Error bars show rms deviation of the QPD signal caused by Brownian motion of the trapped particle. One can conclude that the displacements at the BSW resonance excitation are as large as its Brownian motion magnitude.

In every measurement series, the difference between the QPD signals at the open and closed shutter is calculated. The force value is then determined as the difference multiplied by k and S which are defined through power spectra approximation as described above. A typical example of the QPD sum signal power spectrum is shown in Fig. 8b by grey line. Its approximation by a Lorentzian curve is shown by black.

The maximum force in the direction perpendicular to the surface measured at the BSW resonance is about 100 fN per 1 kW/cm^2 of excitation intensity. The measured value is close to the theoretical prediction for the gradient force obtained with taking into account the angular divergence of 0.4° . The maximum force in the direction of the BSW propagation is about 70 fN per 1 kW/cm^2 of excitation intensity.

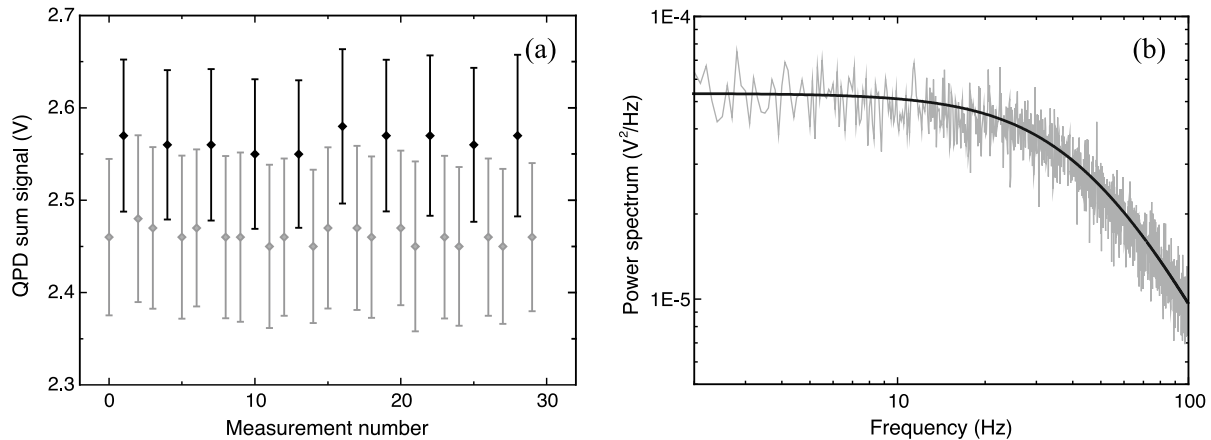


Figure 8. (a) QPD sum signal values measured at the BSW resonance. Black — the excitation radiation is on, grey — excitation is shuttered. Error bars show rms deviation of the QPD signal caused by Brownian motion of the particle in the trap. (b) Typical power spectrum of the QPD sum signal (grey) and its approximation by a Lorentzian curve.

5. CONCLUSIONS

The potential of PFM to directly probe the evanescent field of the BSW in a one-dimensional photonic crystal has been demonstrated. The calculations of the BSW-induced force on a polystyrene microbead have been carried out in the dipole approximation and by numerical FDTD simulations. The force has been shown to be large enough to be measured by PFM. Experimental technique has been developed to perform PFM of the BSW.

ACKNOWLEDGMENTS

This work was supported by the Russian Science Foundation grant #15-12-00065 (experimental) and the Russian Foundation of Basic Research (modelling).

REFERENCES

- [1] Ashkin, A., Dziedzic, J. M., Bjorkholm, J. E., and Chu, S., "Observation of a single-beam gradient force optical trap for dielectric particles," *Opt. Lett.* **11**(5), 288–290 (1986).
- [2] Henon, S., Lenormand, G., Richert, A., and Gallet, F., "A new determination of the shear modulus of the human erythrocyte membrane using optical tweezers," *Biophys. J.* **76**(2), 1145–1151 (1999).
- [3] Xie, C., Dinno, M. A., and Li, Y.-q., "Near-infrared raman spectroscopy of single optically trapped biological cells," *Opt. Lett.* **27**(4), 249–251 (2002).
- [4] Lyubin, E. V., Khokhlova, M. D., Skryabina, M. N., and Fedyanin, A. A., "Cellular viscoelasticity probed by active rheology in optical tweezers," *J. Biomed. Opt.* **17**(10), 101510 (2012).
- [5] Block, S. M., Goldstein, L. S. B., and Schnapp, B. J., "Bead movement by single kinesin molecules studied with optical tweezers," *Nature* **348**, 348–352 (1990).
- [6] Nishizaka, T., Miyata, H., Yoshikawa, H., Ishiwata, S., and Kinoshita Jr, K., "Unbinding force of a single motor molecule of muscle measured using optical tweezers," *Nature* **377**(6546), 251–254 (1995).
- [7] Wang, M. D., Yin, H., Landick, R., Gelles, J., and Block, S. M., "Stretching dna with optical tweezers," *Biophys. J.* **72**(3), 1335–1346 (1997).
- [8] Schäffer, E., Nørrelykke, S. F., and Howard, J., "Surface forces and drag coefficients of microspheres near a plane surface measured with optical tweezers," *Langmuir* **23**(7), 3654–3665 (2007).
- [9] Beunis, F., Strubbe, F., Neyts, K., and Petrov, D., "Beyond millikan: the dynamics of charging events on individual colloidal particles," *Phys. Rev. Lett.* **108**(1), 016101 (2012).
- [10] Helseth, L. E., "Paramagnetic particles in an optical trap," *Opt. Commun.* **276**(2), 277–282 (2007).

- [11] Romodina, M. N., Khokhlova, M. D., Lyubin, E. V., and Fedyanin, A. A., "Direct measurements of magnetic interaction-induced cross-correlations of two microparticles in brownian motion," *Sci. Rep.* **5**, 10491 (2015).
- [12] Dufresne, E. R. and Grier, D. G., "Optical tweezer arrays and optical substrates created with diffractive optics," *Rev. Sci. Instrum.* **69**(5), 1974–1977 (1998).
- [13] Mio, C., Gong, T., Terray, A., and Marr, D. W. M., "Design of a scanning laser optical trap for multiparticle manipulation," *Rev. Sci. Instrum.* **71**(5), 2196–2200 (2000).
- [14] Curtis, J. E., Koss, B. A., and Grier, D. G., "Dynamic holographic optical tweezers," *Opt. Commun.* **207**(1), 169–175 (2002).
- [15] Erickson, D., Serey, X., Chen, Y.-F., and Mandal, S., "Nanomanipulation using near field photonics," *Lab Chip* **11**(6), 995–1009 (2011).
- [16] Kawata, S. and Sugiura, T., "Movement of micrometer-sized particles in the evanescent field of a laser beam," *Opt. Lett.* **17**(11), 772–774 (1992).
- [17] Kawata, S. and Tani, T., "Optically driven mie particles in an evanescent field along a channeled waveguide," *Opt. Lett.* **21**(21), 1768–1770 (1996).
- [18] Brambilla, G., Murugan, G. S., Wilkinson, J. S., and Richardson, D. J., "Optical manipulation of microspheres along a subwavelength optical wire," *Opt. Lett.* **32**(20), 3041–3043 (2007).
- [19] Righini, M., Volpe, G., Girard, C., Petrov, D., and Quidant, R., "Surface plasmon optical tweezers: tunable optical manipulation in the femtonewton range," *Phys. Rev. Lett.* **100**(18), 186804 (2008).
- [20] Wang, K., Schonbrun, E., and Crozier, K. B., "Propulsion of gold nanoparticles with surface plasmon polaritons: evidence of enhanced optical force from near-field coupling between gold particle and gold film," *Nano Lett.* **9**(7), 2623–2629 (2009).
- [21] Wang, K., Schonbrun, E., Steinvurzel, P., and Crozier, K. B., "Scannable plasmonic trapping using a gold stripe," *Nano Lett.* **10**(9), 3506–3511 (2010).
- [22] Mandal, S., Serey, X., and Erickson, D., "Nanomanipulation using silicon photonic crystal resonators," *Nano Lett.* **10**(1), 99–104 (2009).
- [23] Descharmes, N., Dharanipathy, U. P., Diao, Z., Tonin, M., and Houdré, R., "Single particle detection, manipulation and analysis with resonant optical trapping in photonic crystals," *Lab Chip* **13**(16), 3268–3274 (2013).
- [24] Grigorenko, A. N., Roberts, N. W., Dickinson, M. R., and Zhang, Y., "Nanometric optical tweezers based on nanostructured substrates," *Nature Photon.* **2**(6), 365–370 (2008).
- [25] Yeh, P., Yariv, A., and Cho, A. Y., "Optical surface waves in periodic layered media," *Appl. Phys. Lett.* **32**(2), 104–105 (1978).
- [26] Robertson, W. M. and May, M. S., "Surface electromagnetic wave excitation on one-dimensional photonic band-gap arrays," *Appl. Phys. Lett.* **74**(13), 1800–1802 (1999).
- [27] Villa, F., Regalado, L. E., Ramos-Mendieta, F., Gaspar-Armenta, J., and Lopez-Ríos, T., "Photonic crystal sensor based on surface waves for thin-film characterization," *Opt. Lett.* **27**(8), 646–648 (2002).
- [28] Descrovi, E., Frascella, F., Sciacca, B., Geobaldo, F., Dominici, L., and Michelotti, F., "Coupling of surface waves in highly defined one-dimensional porous silicon photonic crystals for gas sensing applications," *Appl. Phys. Lett.* **91**(24), 241109 (2007).
- [29] Li, Y., Yang, T., Song, S., Pang, Z., Du, G., and Han, S., "Phase properties of bloch surface waves and their sensing applications," *Appl. Phys. Lett.* **103**(4), 041116 (2013).
- [30] Sfez, T., Descrovi, E., Yu, L., Quaglio, M., Dominici, L., Nakagawa, W., Michelotti, F., Giorgis, F., and Herzig, H. P., "Two-dimensional optics on silicon nitride multilayer: refraction of bloch surface waves," *Appl. Phys. Lett.* **96**(15), 151101 (2010).
- [31] Yu, L., Barakat, E., Sfez, T., Hvozdar, L., Di Francesco, J., and Herzig, H. P., "Manipulating bloch surface waves in 2d: a platform concept-based flat lens," *Light: Sci. Appl.* **3**(1), e124 (2014).
- [32] Ghislain, L. P. and Webb, W. W., "Scanning-force microscope based on an optical trap," *Opt. Lett.* **18**(19), 1678–1680 (1993).
- [33] Florin, E.-L., Pralle, A., Hörber, J. K. H., and Stelzer, E. H. K., "Photonic force microscope based on optical tweezers and two-photon excitation for biological applications," *J. Struct. Biol.* **119**(2), 202–211 (1997).

- [34] Wada, K.-i., Sasaki, K., and Masuhara, H., “Optical measurement of interaction potentials between a single microparticle and an evanescent field,” *Appl. Phys. Lett.* **76**(20), 2815–2817 (2000).
- [35] Volpe, G., Quidant, R., Badenes, G., and Petrov, D., “Surface plasmon radiation forces,” *Phys. Rev. Lett.* **96**(23), 238101 (2006).
- [36] Volpe, G., Quidant, R., Petrov, D. V., and Badenes, G., “Measurement of radiation forces generated by plasmon fields,” *Proc. SPIE* 5930 (2005).
- [37] Tlustý, T., Meller, A., and Bar-Ziv, R., “Optical gradient forces of strongly localized fields,” *Phys. Rev. Lett.* **81**(8), 1738–1741 (1998).
- [38] Jákł, P., Šerý, M., Ježek, J., Jonáš, A., Liška, M., and Zemánek, P., “Behaviour of an optically trapped probe approaching a dielectric interface,” *J. Mod. Opt.* **50**(10), 1615–1625 (2003).
- [39] Shilkin, D. A., Lyubin, E. V., Soboleva, I. V., and Fedyanin, A. A., “Trap position control in the vicinity of reflecting surfaces in optical tweezers,” *JETP Lett.* **98**(10), 644–647 (2014).
- [40] Berg-Sørensen, K. and Flyvbjerg, H., “Power spectrum analysis for optical tweezers,” *Rev. Sci. Instrum.* **75**(3), 594–612 (2004).
- [41] Kazoe, Y. and Yoda, M., “Measurements of the near-wall hindered diffusion of colloidal particles in the presence of an electric field,” *Appl. Phys. Lett.* **99**(12), 124104 (2011).